symmetry

MDPI

*Article*

# Computational Study of $H_2$ Catalytic Combustion on $Pd_{38}$ Cluster Model and Pd(111) Slab Model

**Dabin Qi [1], Xudong Luo [1,*], Yulong Yao [2], Na Qi [3], Xiaojun Lu [1], Hao Chen [4] and Hongqi Shi [4]**

[1] School of Applied Technology, University of Science and Technology Liaoning, Anshan 114000, China; qdbinner@163.com (D.Q.); 591kfc@163.com (X.L.)
[2] Fushun Petrochemical Company of PetroChina, Fushun 113000, China; yaoyulong@petrochina.com
[3] Liaoning Provincial Big Data Management Center, Shenyang 110000, China; qidabin2022@163.com
[4] Wuhan Second Ship Design and Research Institute, Wuhan 430064, China; 19chenhao86@163.com (H.C.); shi_hong_qi@163.com (H.S.)
* Correspondence: luoxudong2019@sina.com

**Abstract:** Hydrogen is one of the exhaust gases produced by nuclear power stations. Due to the potential danger of incomplete combustion and the emission of hydrogen, hydrogen catalytic combustion is introduced to ensure the safety of nuclear power stations. Palladium is a widely used catalyst for hydrogen catalytic combustion. $H_2$ catalytic combustion on a Pd(111) slab model and $Pd_{38}$ cluster model were simulated using density functional theory (DFT), in order to analyze the $H_2$ oxidation mechanism on the catalyst surface.

**Keywords:** density functional theory calculation; $H_2$ catalytic combustion; slab model; cluster model



**Citation:** Qi, D.; Luo, X.; Yao, Y.; Qi, N.; Lu, X.; Chen, H.; Shi, H. Computational Study of $H_2$ Catalytic Combustion on $Pd_{38}$ Cluster Model and Pd(111) Slab Model. *Symmetry* **2022**, *14*, 1544. https://doi.org/10.3390/sym14081544

Academic Editor: György Keglevich

Received: 22 May 2022
Accepted: 19 July 2022
Published: 28 July 2022



## 1. Introduction

Hydrogen, $H_2$, is one of the exhaust gases produced by nuclear power stations. In nuclear power stations, large amounts of hydrogen are released into the containment vessel after a coolant loss. $H_2$ is a flammable and explosive gas. An $H_2$ concentration at 4–75.6% (volume concentration) will trigger an explosion when encountering a fire source, which would result in a serious accident. Therefore, the hydrogen produced by a nuclear power station needs to be treated in a timely manner. Many methods of hydrogen elimination have been applied in nuclear power station. $H_2$ catalytic combustion can reduce the $H_2$ concentration, to improve the safety performance of nuclear power stations. One advantage of $H_2$ catalytic combustion is that it can eliminate hydrogen at low concentrations. Another is that $H_2$ catalytic combustion can function at room temperature.

$H_2$ catalytic combustion is a flameless combustion. As early as 1970, Pfefferle studied catalytic combustion [1]. Compared to conventional combustion, catalytic combustion has a higher efficiency, less pollutants, and it is easier to control the combustion temperature. $H_2$ catalytic combustion was first studied by Sharer [2]. Subsequently, Kramer et al. studied low-temperature $H_2$ catalytic combustion on a Pd catalyst [3]. Zhang et al. reported the activity of a Pt catalyst for $H_2$ low-temperature catalytic combustion [4]. From then on, many works on $H_2$ catalytic combustion have been studied by researchers [4–6]. So far, Pt [7–14] and Pd [15–17] catalysts have been commonly applied for $H_2$ catalytic combustion. The catalytic reaction of $H_2$ and $O_2$ is a basic catalytic oxidation reaction. It is of great significance to select an appropriate catalyst for a heterogeneous catalytic combustion, by studying the adsorption mechanism of reactant molecules on the catalyst surface, especially the reaction rate of reactants on the catalytic sites and the adsorption/desorption effect of the catalytic surface [18].

With the development of modern computers, computational chemistry has made a great deal of progress. Sui et al. studied the $H_2$ catalytic oxidation reaction mechanism on a PdO surface using density functional theory (DFT) [19]. $H_2$ firstly dissociates into

adsorbed H on the PdO surface, with an activation energy of 58.6 kJ/mol. Then, the H atom reacts with the O atom in PdO to form OH. Finally, two OH react to form $H_2O$ and O, with an activation energy of 58.9 kJ/mol. Qi et al. investigated $H_2$ catalytic combustion on Pt(111) surfaces [18]. At first, $H_2$ and $O_2$ dissociate into adsorbed H and O on the Pt surface, respectively. Then, H and O react to form OH. Finally, OH reacts with H to form $H_2O$. At present, few literature works have systematically studied the mechanism of $H_2$ catalytic combustion using DFT. It is necessary to study the reaction mechanism of $H_2$ catalytic combustion on a Pd metal surface, which is helpful to guide the selection of a catalyst.

In many previous works, the researchers found that the size of particles played an important role in the catalytic system. Tsamis' group studied the efficiency of Pd-doped porous silicon as a catalyst for hydrogen dissociation [20]. It was found that the catalytic activity of Pd-doped porous silicon was significantly higher than that of a planar surface covered with Pd. Abate [21] studied the effect of the size of Pd particles in $H_2O_2$ synthesis. They found that smaller particles of Pd showed a higher rate of combustion. In Huang's work [22], they studied the influence of the size of Pd particles on Heck reactions. Their work showed that the size of the supported Pd particles were smaller, and the catalytic activity was higher. In this work, we wanted to investigate the effect of particle size on $H_2$ catalytic combustion using DFT calculation. A $Pd_{38}$ cluster model simulated the small Pd particles and a Pd(111) slab model simulated the large particles in the catalytic system. Comparing the reaction energy barrier of $H_2$ catalytic combustion on the surface of the two models, the influence of model morphology on the catalytic activity was studied. This method can guide the design of a catalyst rationally, through theoretical calculation, so that catalysts can be designed and prepared more efficiently.

## 2. Computing Method

The DMol3 module of Materials Studio software was applied for DFT calculation of $H_2$ catalytic combustion [23]. In this work, the exchange-correlation energy was calculated using the Perdew–Burke–Ernzerf (PBE) function with generalized gradient approximation (GGA). The wave functions were calculated using a localized double-numerical quality basis set with a polarization d-function (DNP). The effective core potential (ECP) was applied to represent the core electrons of the Pd metal atoms. The k-point mesh was set to $3 \times 3 \times 1$ using Monkhorst–Pack with a thermal smearing of 0.005 hartree. In the configuration optimization, the convergences of the energy, maximum force, and maximum displacement were set as $2.0 \times 10^{-5}$ Ha, 0.004 Ha/Å, and 0.005 Å, respectively. The van der Waals (vdW) interactions were performed using the empirical correction scheme of Grimme (DFT-D).

The transition states (TS) of the elementary reactions used a complete linear synchronous transit and quadratic synchronous transit (LST/QST) approach. The LST method applied a single interpolation to the maximum energy. The QST method searched for an energy maximum with constrained minimizations, to refine the transition states involved in the reaction. In addition, the transition states were optimized by imaginary frequency calculations, in order to confirm that every transition state led to the desired reactants and products [24,25].

The adsorption energy ($E_{ads}$) for adsorbate on Pd surfaces was calculated as follows:

$$E_{ads} = E_{A/Pd} - E_{Pd} - E_{A(g)}$$

where $E_{A/Pd}$ is the total energy of Pd model with an adsorbate; $E_{Pd}$ is the energy of the Pd model; $E_{A(g)}$ is the energy of the adsorbate in gas-phase.

The activation energy ($E_a$) and reaction energy ($\Delta E$):

$$E_a = E_{TS} - E_{IS} \Delta E = E_{FS} - E_{IS}$$

$E_{TS}$ is the free energy of the transition state, $E_{IS}$ is the free energy of the initial state, and $E_{FS}$ is the free energy of final state.

## 3. Results and Discussion

### *3.1. Pd Catalyst Model*

Based on our previous work [26], two models of Pd catalyst, a $Pd_{38}$ cluster model and a Pd(111) slab model, were built. The calculated lattice constant of bulk Pd was 3.90 Å, which is in good agreement with the previous experimental value of 3.62 Å [27]. In Figure 1a, a Pd(111) slab model was constructed as a four-layer symmetric periodic slab. The bottom two layers of the slab were fixed at their original atomic positions in the bulk, while the uppermost two layers and the adsorbates were allowed to relax during structural optimization. The crystal face of the Pd slab surface was a Pd(111) surface, and the vacuum thickness of 12 Å between clean slabs was established, to separate the interactions between the periodically repeating slabs using a 3 × 3 surface unit cell. In Figure 1b, the $Pd_{38}$ cluster was optimized to model Pd particles because the cluster model is more similar to Pd particles than the Pd slab. The $Pd_{38}$ cluster with 14 surfaces was constituted by 38 Pd atoms. The potential adsorption sites are marked in the two models.

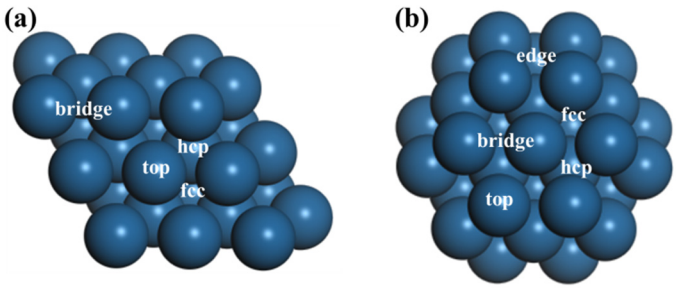


**Figure 1.** Two models of Pd catalysts: (**a**) Pd slab model; (**b**) $Pd_{38}$ cluster model.

### *3.2. Reactants and Intermediates on the $Pd_{38}$ Cluster Model and Pd(111) Slab Model*

The adsorption behaviors of $H_2$ and its reaction intermediates in the two Pd models were investigated, to study the $H_2$ catalytic combustion mechanism. The adsorption geometry of reactants, intermediates, and products in the $Pd_{38}$ cluster model and Pd(111) slab model are shown in Figures 2 and 3, respectively. Tables 1 and 2 list the corresponding adsorption energies of the reactants, intermediates, and products in the $Pd_{38}$ cluster model and Pd(111) slab model, respectively.

The $H_2$ adsorption in the Pd(111) slab model exhibits four structures in Figure 2a(1)–a(4). In Figure 2a(1), the $H_2$ adsorbed on the top site of the Pd(111) slab model, marked as $H_2$-top, with an adsorption energy of −1.31 eV. The lengths of H-Pd bonds were 1.762 Å and 1.760 Å, respectively. In Figure 2a(2), $H_2$ adsorbs on the bridge site of the Pd(111) slab model, marked as the $H_2$-top, with an adsorption energy of −1.43 eV. One H atom adsorbs on a Pd atom and anther H atom adsorbs on the adjacent Pd atom. The lengths of H-Pd bonds were 1.788 Å and 1.792 Å, respectively. In Figure 2a(3), $H_2$ adsorbs on the fcc site of the Pd(111) slab model, marked as $H_2$-fcc. The corresponding adsorption energy was −1.66 eV. The lengths of the H-Pd bonds were 1.798 Å, 1.799 Å, and 1.799 Å, respectively. In Figure 2a(4), the adsorption structure is marked as $H_2$-hcp, where $H_2$ adsorbs on the fcc site of the Pd(111) slab model. The corresponding adsorption energy was −1.62 eV, which is close to that of $H_2$-fcc. The lengths of the H-Pd bonds were 1.802 Å, 1.801 Å, and 1.801 Å, respectively. Compared to the four adsorption structures, the adsorption energies were from 1.31 eV to 1.66 eV. This indicates that the four adsorption structures were stable. The adsorption energy of $H_2$-fcc was lowest of the four adsorption structures, which indicates that $H_2$ prefers to adsorb on the fcc site of the Pd(111) surface. Figure 2b(1)–b(4) shows the adsorption structures of $O_2$ on the Pd(111) surface. Similarly to the $H_2$ adsorption on the Pd(111) surface, there were also four adsorption structures of $O_2$ on the Pd(111) surface. $O_2$ can also adsorb on the top, bridge, fcc, and hcp sites; marked as $O_2$-top, $O_2$-bridge, $O_2$-fcc, and $O_2$-hcp, respectively. The corresponding adsorption energies were −0.68 eV, −0.77 eV, −0.98 eV, and −0.95 eV, respectively. It can be seen that $O_2$-fcc was the most stable adsorption structure, with the lowest adsorption energy. Figure 2c(1)–c(4) shows the H adsorption structures on the Pd(111)

surface. H adsorbs on the top, bridge, fcc, and hcp sites, with adsorption energies of −2.08 eV, −2.49 eV, −2.57 eV, and −2.54 eV, respectively. H-fcc is the most stable adsorption structure, with the lowest adsorption energy of −2.57 eV. The O adsorption structures on the top, bridge, fcc, and hcp site are shown in Figure 2d(1)–d(4). The corresponding adsorption energies of the four structures were −2.37 eV, −3.06 eV, −3.25 eV, and −2.96 eV, respectively. The OH adsorption structures on the top, bridge, fcc, and hcp site are shown in Figure 2e(1)–e(4). The corresponding adsorption energies of the four structures were −1.03 eV, −1.39 eV, −1.40 eV, and −1.33 eV, respectively. In Figure 2f(1),f(2), $H_2O$ adsorbs on the top and bridge site of the Pd(111) surface, with adsorption energies of −0.36 eV and −0.59 eV, respectively. According to the calculation results, the fcc site on the Pd(111) surface is beneficial for adsorption.

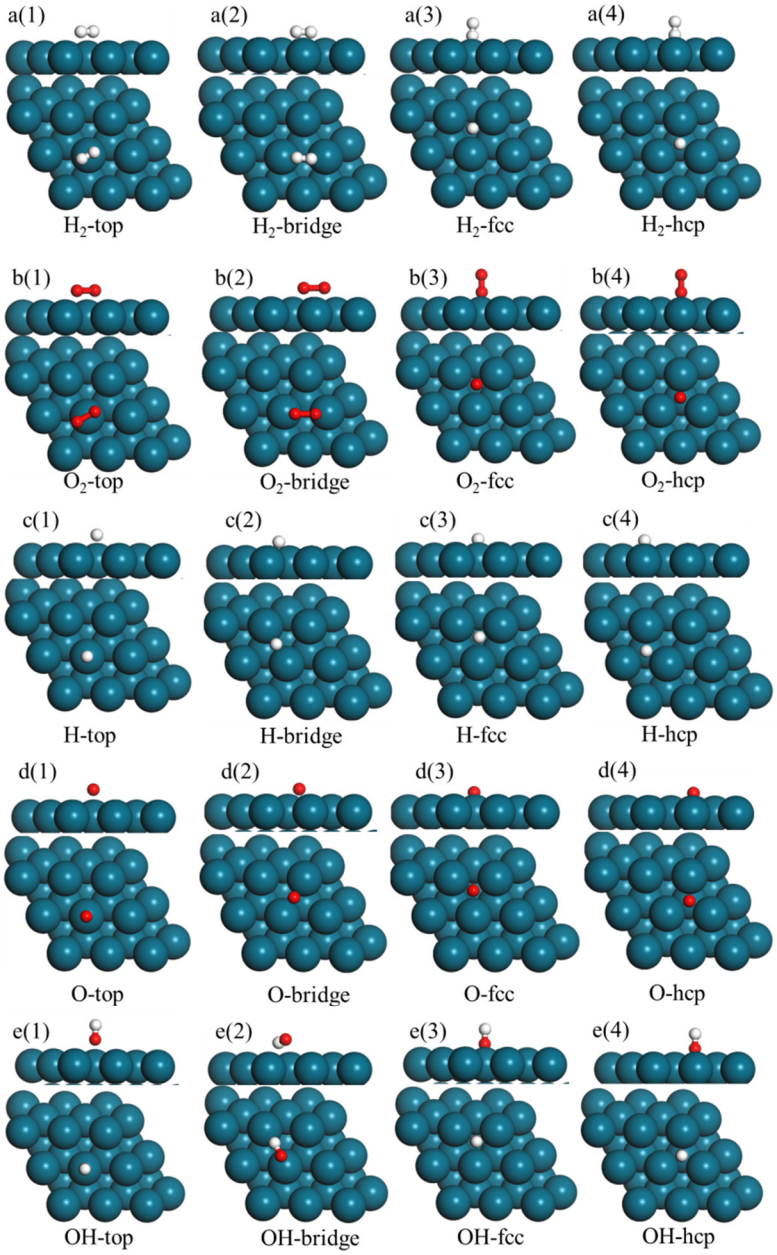


**Figure 2.** *Cont.*

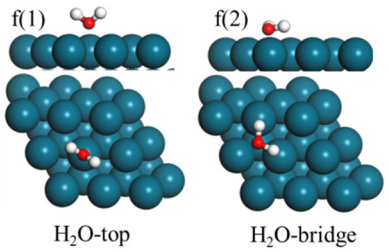


**Figure 2.** Adsorption configurations of all intermediates involved in the $H_2$ combustion reaction on the Pd(111) surface. (**a(1)**) $H_2$-top adsorption; (**a(2)**) $H_2$-bridge adsorption; (**a(3)**) $H_2$-fcc adsorption; (**a(4)**) $H_2$-hcp adsorption; (**b(1)**) $O_2$-top adsorption; (**b(2)**) $O_2$-bridge adsorption; (**b(3)**) $O_2$-fcc adsorption; (**b(4)**) $O_2$-hcp adsorption; (**c(1)**) H-top adsorption; (**c(2)**) H-bridge adsorption; (**c(3)**) H-fcc adsorption; (**c(4)**) H-hcp adsorption; (**d(1)**) O-top adsorption; (**d(2)**) O-bridge adsorption; (**d(3)**) O-fcc adsorption; (**d(4)**) O-hcp adsorption; (**e(1)**) OH-top adsorption; (**e(2)**) OH-bridge adsorption; (**e(3)**) OH-fcc adsorption; (**e(4)**) OH-hcp adsorption; (**f(1)**) $H_2O$-top adsorption; (**f(2)**) $H_2O$-bridge adsorption; Here, O, H, and Pd atoms are shown as red, white and blue balls, respectively, which are the same in Figures 2–5.

Figure 3 shows the adsorption structures of adsorbates in the $Pd_{38}$ cluster model. $H_2$ adsorbs on the $Pd_{38}$ cluster model shown in Figure 3a(1)–a(5). In Figure 3a(1)–a(4), $H_2$ adsorption on the (111) surface of the $Pd_{38}$ cluster is similar to that on the Pd(111) slab model. $H_2$ adsorbs on the top, bridge, fcc, and hcp site, with adsorption energies of −1.34 eV, −1.55 eV, −1.76 eV, and −1.73 eV, respectively. Compared to that on the Pd(111) slab model, the adsorption energies of $H_2$ on the $Pd_{38}$ cluster model are lower than that of $H_2$ on the Pd(111) slab model. This indicates that $H_2$ prefers to adsorb on the $Pd_{38}$ cluster model instead of the Pd(111) surface. In Figure 3a(5), $H_2$ adsorbs on the edge site of the $Pd_{38}$ cluster model, with an adsorption energy of −0.92 eV. The adsorption structures of $O_2$ on the $Pd_{38}$ cluster are shown in Figure 3b(1)–b(5). The adsorption energies of $O_2$ on the top, bridge, fcc, hcp, and edge site of the $Pd_{38}$ cluster were −0.83 eV, −0.95 eV, −1.06 eV, −1.02 eV, and −0.89 eV, respectively. Figure 3c(1)–c(5) shows the adsorption structures of the H atom on the top, bridge, fcc, hcp, and edge site of the $Pd_{38}$ cluster, with adsorption energies of −1.14 eV, −1.38 eV, −1.57 eV, −1.54 eV, and −1.11 eV, respectively. Figure 3d(1)–d(5) shows the adsorption structures of the O atom on the top, bridge, fcc, hcp, and edge site of the $Pd_{38}$ cluster, with adsorption energies of −2.45 eV, −2.59 eV, −3.62 eV, −3.56 eV, and −2.45 eV, respectively. The adsorption structures of OH on the top, bridge, fcc, hcp, and edge site of the $Pd_{38}$ cluster are shown in Figure 3e(1)–e(5). The corresponding adsorption energies were −1.57 eV, −2.51 eV, −2.46 eV, −2.41 eV, and −0.61 eV, respectively. There are three adsorption structures of $H_2O$ on the top, bridge, and edge site of the $Pd_{38}$ cluster. The corresponding adsorption energies were −0.36 eV, −0.59 eV, and −0.44 eV. According to the adsorption energies, adsorbates prefer to adsorb on the $Pd_{38}$ cluster model than on the Pd(111) slab model. As the $Pd_{38}$ cluster model is a better electron donor, the adsorption of the adsorbate is more stable [26].

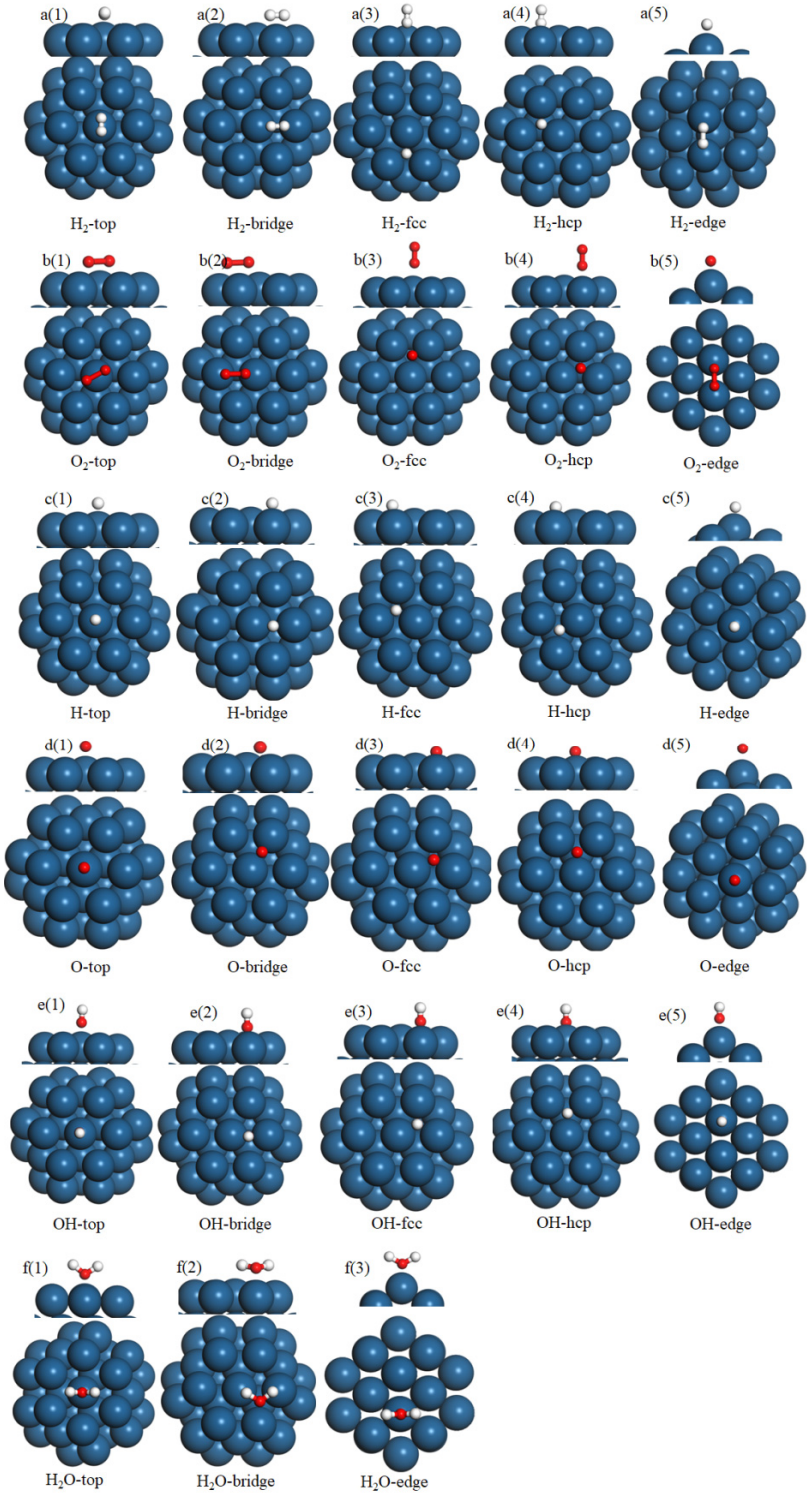


**Figure 3.** Adsorption configurations of all adsorbates involved in the $H_2$ combustion reaction on the $Pd_{38}$ cluster surface. (**a(1)**) $H_2$-top adsorption; (**a(2)**) $H_2$-bridge adsorption; (**a(3)**) $H_2$-fcc adsorption; (**a(4)**) $H_2$-hcp adsorption; (**a(5)**) $H_2$-edge adsorption; (**b(1)**) $O_2$-top adsorption; (**b(2)**) $O_2$-bridge adsorption; (**b(3)**) $O_2$-fcc adsorption; (**b(4)**) $O_2$-hcp adsorption; (**b(5)**) $O_2$-edge adsorption; (**c(1)**) H-top adsorption; (**c(2)**) H-bridge adsorption; (**c(3)**) H-fcc adsorption; (**c(4)**) H-hcp adsorption; (**c(5)**) H-edge adsorption; (**d(1)**) O-top adsorption; (**d(2)**) O-bridge adsorption; (**d(3)**) O-fcc adsorption; (**d(4)**) O-hcp adsorption; (**d(5)**) O-edge adsorption; (**e(1)**) OH-top adsorption; (**e(2)**) OH-bridge adsorption; (**e(3)**) OH-fcc adsorption; (**e(4)**) OH-hcp adsorption; (**e(5)**) OH-edge adsorption; (**f(1)**) $H_2O$-top adsorption; (**f(2)**) $H_2O$-bridge adsorption; (**f(3)**) $H_2O$-edge adsorption.

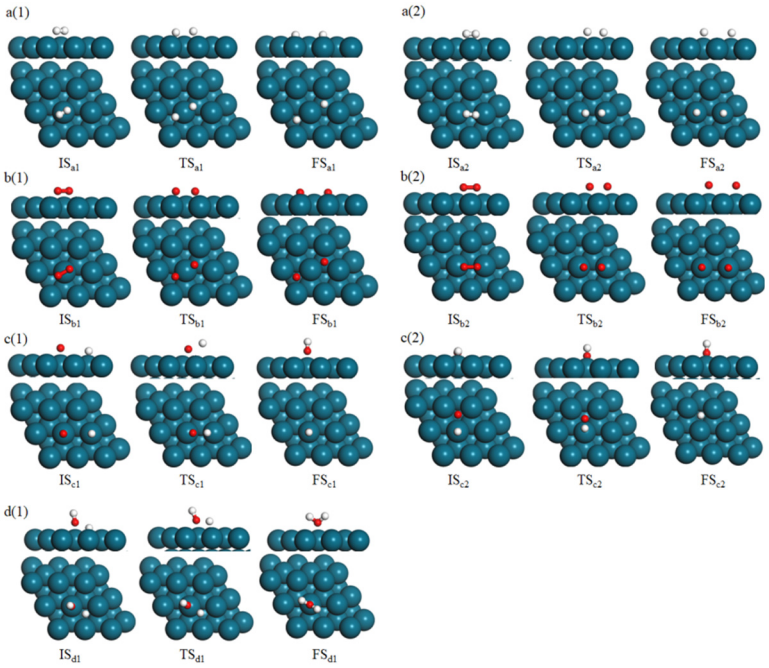


**Figure 4.** Elementary steps of $H_2$ oxidation on the Pd(111) surface: (**a(1)**,**a(2)**) $H_2$ dissociation; (**b(1)**,**b(2)**) $O_2$ dissociation; (**c(1)**,**c(2)**) OH formation; (**d(1)**) $H_2O$ formation.

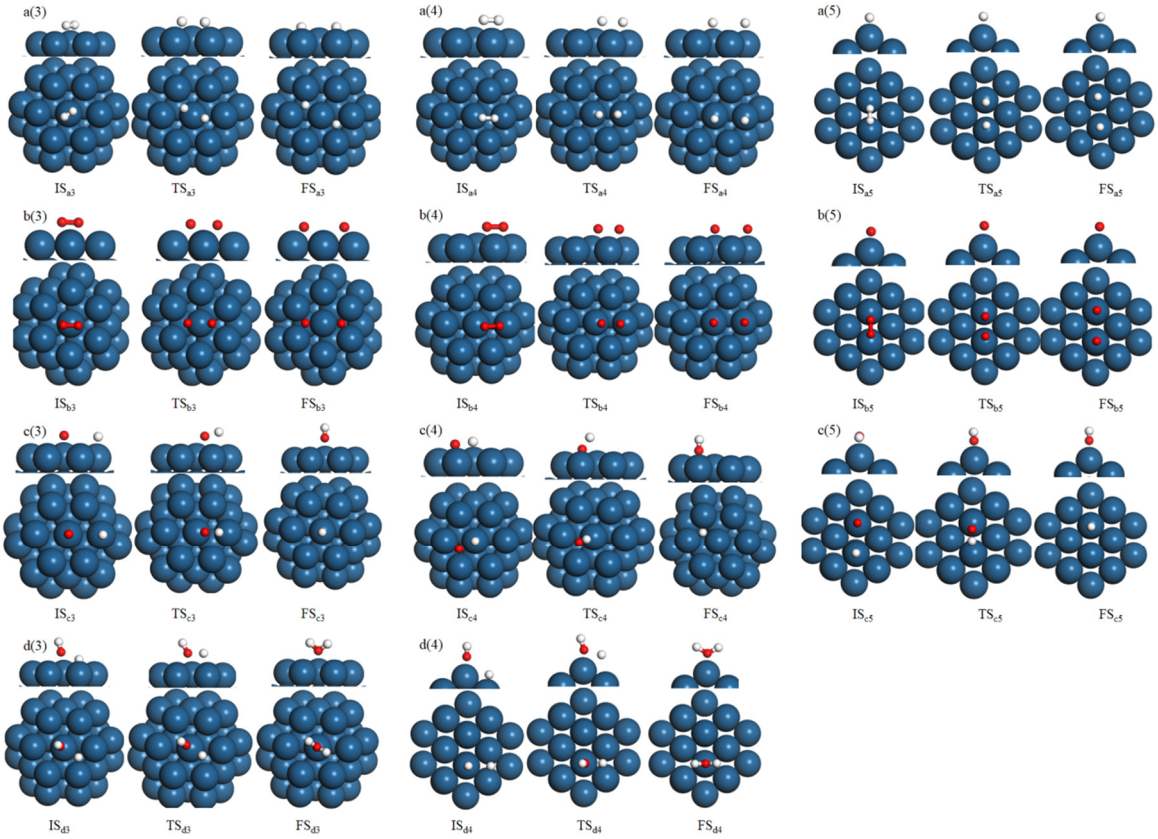


**Figure 5.** Elementary steps of $H_2$ oxidation on the $Pd_{38}$ surface: (**a(3)**,**a(4)**,**a(5)**) $H_2$ dissociation; (**b(3)**,**b(4)**,**b(5)**) $O_2$ dissociation; (**c(3)**,**c(4)**,**c(5)**) OH formation; (**d(3)**,**d(4)**) $H_2O$ formation.

**Table 1.** Geometric parameters and adsorption energies of all adsorbates involved in $H_2$ combustion on the Pd(111) slab surface.

| Figures | Name | Adsorption Energy/eV | Geometric Parameter/Å |
|---|---|---|---|
| Figure 2a(1) | $H_2$-top | −1.31 | Pd1-H1:1.762; Pd1-H2:1.760 |
| Figure 2a(2) | $H_2$-bridge | −1.43 | Pd1-H1:1.788; Pd2-H2:1.792 |
| Figure 2a(3) | $H_2$-fcc | −1.66 | Pd1-H1:1.798; Pd2-H1:1.799; Pd3-H1:1.799 |
| Figure 2a(4) | $H_2$-hcp | −1.62 | Pd1-H1:1.802; Pd2-H1:1.801; Pd3-H1:1.801 |
| Figure 2b(1) | $O_2$-top | −0.68 | Pd1-O1:1.964; Pd1-O 2:1.965 |
| Figure 2b(2) | $O_2$-bridge | −0.77 | Pd1-O1:2.019; Pd2-O 2:2.017 |
| Figure 2b(3) | $O_2$-fcc | −0.98 | Pd1-O 1:1.972; Pd2-O 1:1.970; Pd3-O 1:1.970 |
| Figure 2b(4) | $O_2$-hcp | −0.95 | Pd1-O 1:1.993; Pd2-O1:1.990; Pd3-O1:1.991 |
| Figure 2c(1) | H-top | −2.08 | Pd1-H:1.646 |
| Figure 2c(2) | H-bridge | −2.49 | Pd1-H:1.736; Pd2-H:1.734 |
| Figure 2c(3) | H-fcc | −2.57 | Pd1-H:1.759; Pd2-H:1.760; Pd3-H:1.760 |
| Figure 2c(4) | H-hcp | −2.54 | Pd1-H:1.768; Pd2-H:1.768; Pd3-H:1.769 |
| Figure 2d(1) | O-top | −2.37 | Pd1-O:1.938 |
| Figure 2d(2) | O-bridge | −3.06 | Pd1-O:1.998; Pd2-O:1.998 |
| Figure 2d(3) | O-fcc | −3.25 | Pd1-O:2.034; Pd2-H:2.035; Pd3-O:2.035 |
| Figure 2d(4) | O-hcp | −2.96 | Pd1-O:2.079; Pd2-O:2.079; Pd3-O:2.078 |
| Figure 2e(1) | OH-top | −1.03 | Pd1-O:1.957 |
| Figure 2e(2) | OH-bridge | −1.39 | Pd1-O:2.016; Pd2-O:2.016 |
| Figure 2e(3) | OH-fcc | −1.40 | Pd1-O:2.055; Pd2-H:2.056; Pd3-O:2.055 |
| Figure 2e(4) | OH-hcp | −1.33 | Pd1-O:2.092; Pd2-O:2.093; Pd3-O:2.093 |
| Figure 2f(1) | $H_2O$-top | −0.36 | Pd1-O:2.105 |
| Figure 2f(2) | $H_2O$-bridge | −0.59 | Pd1-H1:1.887; Pd2-H2:1.886 |

**Table 2.** Geometric parameters and adsorption energies of all adsorbates involved in $H_2$ combustion on the $Pd_{38}$ cluster surface.

| Figures | Name | Adsorption Energy/eV | Geometric Parameter/Å |
|---|---|---|---|
| Figure 3a(1) | $H_2$-top | −1.34 | Pd1-H1:1.733; Pd1-H2:1.732 |
| Figure 3a(2) | $H_2$-bridge | −1.55 | Pd1-H1:1.745; Pd2-H2:1.752 |
| Figure 3a(3) | $H_2$-fcc | −1.76 | Pd1-H1:1.756; Pd2-H1:1.768; Pd3-H1:1.769 |
| Figure 3a(4) | $H_2$-hcp | −1.73 | Pd1-H1:1.781; Pd2-H1:1.794; Pd3-H1:1.795 |
| Figure 3a(5) | $H_2$-edge | −0.92 | Pd1-H1:1.881; Pd2-H2:1.882 |
| Figure 3b(1) | $O_2$-top | −0.83 | Pd1-O1:1.968; Pd1-O2:1.968 |
| Figure 3b(2) | $O_2$-bridge | −0.95 | Pd1-O1:2.114; Pd2-O2:2.121 |
| Figure 3b(3) | $O_2$-fcc | −1.06 | Pd1-O1:2.070; Pd2-O1:2.077; Pd3-O1:2.077 |
| Figure 3b(4) | $O_2$-hcp | −1.02 | Pd1-O1:2.059; Pd2-O1:2.066; Pd3-O1:2.067 |
| Figure 3b(5) | $O_2$-edge | −0.89 | Pd1-O1:1.993; Pd2-O2:1.994 |
| Figure 3c(1) | H-top | −1.14 | Pd1-H:1.630 |
| Figure 3c(2) | H-bridge | −1.38 | Pd1-H:1.724; Pd2-H:1.729 |
| Figure 3c(3) | H-fcc | −1.57 | Pd1-H:1.738; Pd2-H:1.756; Pd3-H:1.754 |
| Figure 3c(4) | H-hcp | −1.54 | Pd1-H:1.749; Pd2-H:1.752; Pd3-H:1.750 |
| Figure 3c(5) | H-edge | −1.11 | Pd1-H:1.688 |
| Figure 3d(1) | O-top | −2.45 | Pd1-O:1.920 |
| Figure 3d(2) | O-bridge | −2.59 | Pd1-O:1.974; Pd2-O:1.979 |
| Figure 3d(3) | O-fcc | −3.62 | Pd1-O:2.011; Pd2-H:2.017; Pd3-O:2.018 |
| Figure 3d(4) | O-hcp | −3.56 | Pd1-O:2.062; Pd2-O:2.074; Pd3-O:2.073 |
| Figure 3d(5) | O-edge | −1.73 | Pd1-O:2.122 |

**Table 2.** *Cont.*

| Figures | Name | Adsorption Energy/eV | Geometric Parameter/Å |
|---|---|---|---|
| Figure 3e(1) | OH-top | −1.57 | Pd1-O:1.924 |
| Figure 3e(2) | OH-bridge | −2.51 | Pd1-O:2.001; Pd2-O:2.009 |
| Figure 3e(3) | OH-fcc | −2.46 | Pd1-O:2.022; Pd2-H:2.028; Pd3-O:2.029 |
| Figure 3e(4) | OH-hcp | −2.41 | Pd1-O:2.069; Pd2-O:2.077; Pd3-O:2.078 |
| Figure 3e(5) | OH-edge | −0.61 | Pd1-O:2.143 |
| Figure 3f(1) | $H_2O$-top | −0.36 | Pd1-O:2.075 |
| Figure 3f(2) | $H_2O$-bridge | −0.59 | Pd1-H1:1.869; Pd2-H2:1.869 |
| Figure 3f(3) | $H_2O$-edge | −0.44 | Pd1-H1:1.869; Pd2-H2:1.869 |

### *3.3. Reaction Mechanism of $H_2$ Catalytic Combustion on $Pd_{38}$ Cluster Model and Pd(111) Slab Model*

The adsorption structure of $H_2$ catalytic combustion on the Pd(111) slab model and $Pd_{38}$ cluster model was optimized, in order to analyze the $H_2$ catalytic combustion mechanism on these two surface models. Figures 4 and 5 show the $H_2$ catalytic combustion reaction on the Pd(111) slab model and $Pd_{38}$ cluster model, respectively. The corresponding activation energies are shown in Figure 6. Table 3 shows the activation energies and reaction energies of the elementary reaction steps.

The $H_2$ dissociation process on the Pd(111) surface is shown in Figure 4a(1). The $H_2$ is first adsorbed at the top site of the Pd(111) surface. As the reaction progresses, the length of the H-H bond is gradually elongated. Finally, the two H atoms gradually move to the hcp site on the Pd(111) surface. This elementary step is an exothermic reaction, with a reaction energy of −0.12 eV. The corresponding activation energy was 0.45 eV, which indicates that the elemental reaction proceeded relatively easily in both kinetics and thermodynamics. Another $H_2$ dissociation process on the Pd(111) surface is shown in Figure 4a(2). $H_2$ first adsorbs at the bridge site on the Pd(111) surface. The H-H bond length is gradually elongated as the reaction progresses. Then, two H atoms are gradually adsorbed to the top site of the two adjacent Pd atoms, respectively. The corresponding activation energy and reaction energy were 0.83 eV and −0.22 eV, respectively. The activation energy of this step was slightly higher than that in Figure 4a(1), which indicates that the $H_2$ dissociation process on the Pd(111) surface prefers to proceed in Figure 4a(2). Similar to the two steps of $H_2$ dissociation on the Pd(111) surface, two $O_2$ dissociation steps on the Pd(111) surface are shown in Figure 4 (b(1),b(2). The activation energies of the two $O_2$ dissociation steps were 0.63 eV and 0.94 eV, respectively. The corresponding reaction energies were −0.47 eV and −0.32 eV, respectively. The OH formation steps are shown in Figure 4c(1),c(2). In Figure 4c(1), H and O are adsorbed on the top site of the Pd(111) surface. As the reaction continues, O and H atoms become closer and bond to form OH. After the reaction, the OH adsorbs on the top site of the Pd(111) surface. The activation energy and reaction energy of the elemental step were 0.57 eV and −0.31 eV, respectively. In Figure 4c(2), the H atom adsorbs at the top site of the Pd(111) surface and the O atom adsorbs at the fcc site of Pd(111) surface. As the reaction progresses, the H atom gradually approaches the O atom to form OH, which adsorbs on the fcc site of the Pd(111) surface. The activation energy and reaction energy were 0.62 eV and −0.19 eV, respectively. Figure 4d(1) shows the elementary step of $H_2O$ formation on the Pd(111) surface. OH adsorbs at the top site of Pd surface and H atom adsorbs at the adjacent fcc site. H atom bonds approaches the O atom in OH, to form $H_2O$, which adsorbs at the top site of the Pd(111) surface. The corresponding reaction activation energy and reaction energy were 0.42 eV and −0.44 eV.

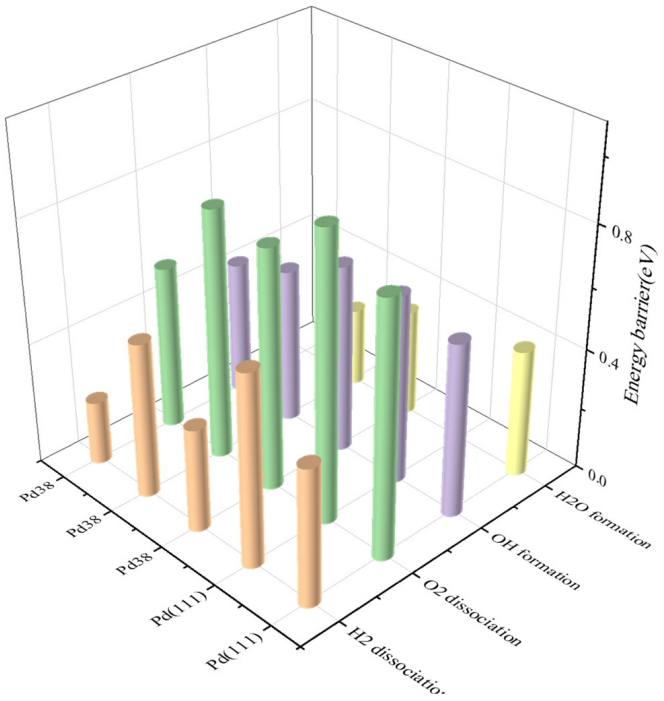


**Figure 6.** Energy barriers of $H_2$ catalytic combustion on the $Pd_{38}$ cluster and Pd(111) slab.

**Table 3.** Activation energies and reaction energies of the $H_2$ catalytic combustion on the $Pd_{38}$ cluster and Pd(111) slab.

| Elementary Step | No. | Pd(111)/(eV) | | $Pd_{38}$/(eV) | | |
|---|---|---|---|---|---|---|
| | | 1 | 2 | 3 | 4 | 5 |
| $H_2 \rightarrow 2H$ | a | $E_a$: 0.45<br>$E_{rxn}$: −0.12 | $E_a$: 0.63<br>$E_{rxn}$: −0.22 | $E_a$: 0.34<br>$E_{rxn}$: −0.23 | $E_a$: 0.51<br>$E_{rxn}$: −0.29 | $E_a$: 0.21<br>$E_{rxn}$: −0.32 |
| $O_2 \rightarrow 2O$ | b | $E_a$: 0.83<br>$E_{rxn}$: −0.47 | $E_a$: 0.94<br>$E_{rxn}$: −0.32 | $E_a$: 0.79<br>$E_{rxn}$: −0.42 | $E_a$: 0.82<br>$E_{rxn}$: −0.35 | $E_a$: 0.54<br>$E_{rxn}$: −0.50 |
| $H + O \rightarrow OH$ | c | $E_a$: 0.57<br>$E_{rxn}$: −0.31 | $E_a$: 0.62<br>$E_{rxn}$: −0.19 | $E_a$: 0.62<br>$E_{rxn}$: −0.33 | $E_a$: 0.51<br>$E_{rxn}$: −0.24 | $E_a$: 0.44<br>$E_{rxn}$: −0.32 |
| $OH + H \rightarrow H_2O$ | d | $E_a$: 0.42<br>$E_{rxn}$: −0.44 | | $E_a$: 0.62<br>$E_{rxn}$: −0.33 | $E_a$: 0.51<br>$E_{rxn}$: −0.24 | |

The elementary steps of $H_2$ dissociation on the $Pd_{38}$ cluster surface are shown in Figure 5a(3)–a(5). The $H_2$ dissociation process in Figure 5a(3) is similar to that in Figure 4a(1). $H_2$ first adsorbs at the top site on the surface of the $Pd_{38}$ cluster. Then, two H atoms adsorb at the hcp site on the $Pd_{38}$ cluster surface after dissociation. The corresponding activation energy and reaction energy of the elemental step were 0.34 eV and −0.23 eV, respectively. The $H_2$ dissociation step in Figure 5a(4) is similar to that in Figure 4a(2), with activation and reaction energies of 0.51 eV and −0.29 eV, respectively. In Figure 5a(5), $H_2$ first adsorbs on the edge site of the $Pd_{38}$ cluster surface. Then, H-H is gradually elongated until breakage with the ongoing reaction. Finally, two H atoms dissociate and adsorb on the edge site of $Pd_{38}$ cluster. The activation energy and reaction energy of the elemental step were 0.21 eV and −0.32 eV, respectively. This elementary step in Figure 5a(5) has the lowest activation energy in the five elementary steps (a(1) to a(5) of $H_2$ dissociation. This indicates that $H_2$ dissociates more easily on the edge site of the $Pd_{38}$ cluster. The $O_2$ dissociation steps on the $Pd_{38}$ cluster surface are shown in Figure 5b(3)–b(5). The $O_2$ dissociation steps on the $Pd_{38}$ cluster are shown in Figure 5b(3),b(4) and are similar to those shown in Figure 4b(1),b(2). $O_2$ begins to dissociate from the top site on the $Pd_{38}$ cluster surface in Figure 5b(3), while

$O_2$ dissociates from the bridge site on $Pd_{38}$ cluster surface in Figure 5b(4). The activation energy and reaction energy of the $O_2$ dissociation process in Figure 5b(3) are 0.79 eV and −0.42 eV, respectively. In Figure 5b(4), the activation energy and reaction energy of the $O_2$ dissociation process are 0.82 eV and −0.35 eV, respectively. Figure 5b(5) shows the $O_2$ dissociation step on the edge site of the $Pd_{38}$ cluster, in which two dissociated O atoms adsorb on the edge of the $Pd_{38}$ cluster. The corresponding activation energy and reaction energy were 0.54 eV and −0.50 eV, respectively. Figure 5c(3)–c(5) shows the OH formation process on the $Pd_{38}$ cluster. The OH formation process shown in Figure 5c(3),c(4) is similar to that shown in Figure 4c(1),c(2). As the reaction progresses, the O atom and H atom move closer to each other, to form OH, which vertically adsorbs on the fcc site and hcp site of the $Pd_{38}$ cluster in Figure 5c(3),c(4), respectively. The corresponding activation energy of OH formation on the $Pd_{38}$ cluster is lower than that on Pd(111). The OH formation step on the edge site of the $Pd_{38}$ cluster is shown in Figure 5c(5). The activation energy and reaction energy were 0.44 eV and −0.32 eV, respectively. Figure 5d(3),d(4) shows the $H_2O$ formation step on the $Pd_{38}$ cluster. The formation process of $H_2O$ in Figure 5d(3) is similar to that in Figure 4d(1). The activation energy and reaction energy were 0.62 eV and −0.33 eV, respectively. Figure 5d(4) shows the $H_2O$ formation step on the edge site of $Pd_{38}$ cluster. OH first adsorbs on the edge site and the H atom adsorbs on the fcc site. As the reaction progresses, the H atom approaches the O atom of OH, to form $H_2O$, which adsorbs on the edge of the $Pd_{38}$ cluster.

The activation energies of each elementary reaction step are shown in Figure 6. Compared to the activation energies of each step, the activation energy of $H_2$ catalytic combustion on the $Pd_{38}$ cluster is lower than that on the Pd(111) surface. As seen in Figure 6, the activation energy of the $O_2$ dissociation step is the highest in the four steps, which is the rate-determining step in the $H_2$ catalytic combustion. The lowest activation energy of $O_2$ dissociation was 0.83 eV on the Pd(111) surface and 0.54 eV on $Pd_{38}$ cluster. These results indicate that the $Pd_{38}$ cluster model had a better catalytic activity than the Pd(111) slab model. The results show that $H_2$ catalytic oxidation is easier to carry out on Pd nanoparticles. Pd small cluster particles play an important role in improving the catalytic activity. This result is consistent with Singh's work [6], where a low Pd loading catalyst showed a low activation energy for $H_2$ catalytic combustion. In addition, the activation energy of $H_2$ combustion on the edge site of the $Pd_{38}$ cluster model was lower than that on the other site, which indicates that the defect sites of the catalytic particles are more conducive to the catalytic reaction. The results show that the catalytic activity is related to the dispersion of the catalytic center in the nanoparticles.

## 4. Conclusions

The reaction mechanisms of $H_2$ catalytic combustion on the $Pd_{38}$ cluster model and Pd(111) slab model were investigated using density functional theory. The activation energies of the $H_2$ catalytic combustion in the $Pd_{38}$ cluster model were lower than those in the Pd(111) slab model. Compared to the activation energies, $H_2$ prefers to react on the $Pd_{38}$ cluster model, especially at the edge sites of the $Pd_{38}$ cluster model. The activation energy of the rate-determining step was only 0.54 eV, which was much lower than that in the Pd(111) slab model. This indicates that catalytic activity is highly related to the dispersion of the catalytic center in nanoparticles. The smaller nanoparticles with more marginal defect sites are beneficial for the $H_2$ catalytic combustion. These results provide theoretical guidance for catalyst design for $H_2$ oxidation combustion, which can reduce experimental costs and improve catalytic design efficiency.

**Author Contributions:** Conceptualization, D.Q. and X.L. (Xudong Luo); methodology, D.Q.; software, H.S.; validation, Y.Y.; formal analysis, N.Q.; investigation, X.L. (Xiaojun Lu); resources, Y.Y.; data curation, D.Q.; writing—original draft preparation, D.Q.; writing—review and editing, H.C.; visualization, D.Q.; supervision, X.L. (Xudong Luo); project administration, X.L. (Xudong Luo); funding acquisition, X.L. (Xudong Luo). All authors have read and agreed to the published version of the manuscript.

**Funding:** This work was supported by National Natural Science Foundation of China (NSFC, Grant No. 51772139).

**Institutional Review Board Statement:** Not applicable.

**Informed Consent Statement:** Not applicable.

**Data Availability Statement:** Exclude this statement.

**Conflicts of Interest:** The authors declare no conflict of interest.

## References

1. Pfefferle, W.C. The catalytic combustor—An approach to cleaner combustion (by reaction control in gas turbine engines). *J. Energy* **2012**, *2*, 142–146.
2. Pangborn, J.; Scott, M.; Sharer, J. Technical prospects for commercial and residential distribution and utilization of hydrogen. *Int. J. Hydrogen Energy* **1977**, *2*, 431–445.
3. Kramer, J.F.; Reihani, S.A.S.; Jackson, G.S. Low-temperature combustion of hydrogen on supported Pd catalysts. *Proc. Combust. Inst.* **2002**, *29*, 989–996. [CrossRef]
4. Zhang, C.M.; Zhang, J.; Ma, J.X. Hydrogen catalytic combustion over a $Pt/Ce_{0.6}Zr_{0.4}O_2/MgAl_2O_4$ mesoporous coating monolithic catalyst. *Int. J. Hydrogen Energy* **2012**, *37*, 12941–12946. [CrossRef]
5. Shinde, V.M.; Madras, G. Nanostructured Pd modified $Ni/CeO_2$ catalyst for water gas shift and catalytic hydrogen combustion reaction. *Appl. Catal. B* **2013**, *132*, 28–38. [CrossRef]
6. Singh, S.A.; Vishwanath, K.; Madras, G. Role of Hydrogen and Oxygen Activation over Pt and Pd-Doped Composites for Catalytic Hydrogen Combustion. *ACS Appl. Mater. Interfaces* **2017**, *9*, 19380–19388.
7. Zhou, J.H.; Wang, Y.; Yang, W.J.; Liu, J.Z.; Wang, Z.H.; Cen, K.F. Combustion of hydrogen-air in catalytic micro-combustors made of different material. *Int. J. Hydrogen Energy* **2009**, *34*, 3535–3545. [CrossRef]
8. Du Preez, S.P.; Jones, D.R.; Bessarabov, D.G.; Falch, A.; Quaresma, C.M.D.; Dunnill, C.W. Development of a Pt/stainless steel mesh catalyst and its application in catalytic hydrogen combustion. *Int. J. Hydrogen Energy* **2019**, *44*, 27094–27106. [CrossRef]
9. Fernández, A.; Arzac, G.; Vogt, U.; Hosoglu, F.; Borgschulte, A.; de Haro, M.J.; Montes, O.; Züttel, A. Investigation of a Pt containing washcoat on SiC foam for hydrogen combustion applications. *Appl. Catal. B* **2016**, *180*, 336–343. [CrossRef]
10. Wang, S.; Chen, L.; Niu, F.; Chen, D.; Qin, L.; Sun, X.; Huang, Y. Catalytic combustion of hydrogen for residential heat supply application. *Int. J. Energy Res.* **2016**, *40*, 1979–1985.
11. Fumey, B.; Buetler, T.; Vogt, U.F. Ultra-low NO emissions from catalytic hydrogen combustion. *Appl. Energy* **2018**, *213*, 334–342. [CrossRef]
12. Nguyen, V.N.; Deja, R.; Peters, R.; Blum, L.; Stolten, D. Study of the catalytic combustion of lean hydrogen-air mixtures in a monolith reactor. *Int. J. Hydrogen Energy* **2018**, *43*, 17520–17530. [CrossRef]
13. Arzac, G.M.; Montes, O.; Fernandez, A. Pt-impregnated catalysts on powdery SiC and other commercial supports for the combustion of hydrogen under oxidant conditions. *Appl. Catal. B* **2017**, *201*, 391–399. [CrossRef]
14. Zheng, X.; Mantzaras, J.; Bombach, R. Kinetic interactions between hydrogen and carbon monoxide oxidation over platinum. *Combust. Flame* **2014**, *161*, 332–346. [CrossRef]
15. Han, S.M.; Mullins, C.B. Catalytic Reactions on Pd-Au metallic Model Catalysts. *Accounts Chem. Res.* **2021**, *54*, 379–387. [CrossRef] [PubMed]
16. Morfin, F.; Sabroux, J.C.; Renouprez, A. Catalytic combustion of hydrogen for mitigating hydrogen risk in case of a severe accident in a nuclear power plant: Study of catalysts poisoning in a representative atmosphere. *Appl. Catal. B* **2004**, *47*, 47–58. [CrossRef]
17. Sandeep, K.C.; Bhattacharyya, R.; Warghat, C.; Bhanja, K.; Mohan, S. Experimental investigation on the kinetics of catalytic recombination of hydrogen with oxygen in air. *Int. J. Hydrogen Energy* **2014**, *39*, 17906–17912. [CrossRef]
18. Qi, W.J.; Ran, J.Y.; Wang, R.R.; Du, X.S.; Shi, J.; Ran, M.C. Kinetic mechanism of effects of hydrogen addition on methane catalytic combustion over Pt(111) surface: A DFT study with cluster modeling. *Comput. Mater. Sci.* **2016**, *111*, 430–442. [CrossRef]
19. Sui, R.; Liang, W.K.; Zhang, L.; Mantzaras, J.; Law, C.K. Kinetic interactions between H-2 and CO in catalytic oxidation over PdO. *Combust. Flame* **2020**, *211*, 270–280. [CrossRef]
20. Tsamis, C.; Tsoura, L.; Nassiopoulou, A.; Travlos, A.; Salmas, C.; Hatzilyberis, K.; Androutsopoulos, G. Hydrogen catalytic oxidation reaction on Pd-doped porous silicon. *IEEE Sens. J.* **2002**, *2*, 89–95. [CrossRef]
21. Abate, S.; Barbera, K.; Centi, G.; Giorgianni, G.; Perathoner, S. Role of size and pretreatment of Pd particles on their behaviour in the direct synthesis of $H_2O_2$. *J. Energy Chem.* **2016**, *25*, 9. [CrossRef]
22. Huang, L.; Wang, Z.; Tan, J. New insights into catalysis for Heck reactions with fine supported Pd particles. *React. Chem. Eng.* **2020**, *5*, 921–934. [CrossRef]
23. Chen, H.; Wu, Y.L.; Qi, S.T.; Chen, Y.; Yang, M.D. Deoxygenation of octanoic acid catalyzed by hollow spherical $Ni/ZrO_2$. *Appl. Catal. A* **2017**, *529*, 79–90. [CrossRef]
24. Wang, B.J.; Song, L.Z.; Zhang, R.G. The dehydrogenation of CH4 on Rh(111), Rh(110) and Rh(100) surfaces: A density functional theory study. *Appl. Surf. Sci.* **2012**, *258*, 3714–3722. [CrossRef]

25. Zhang, R.G.; Song, L.Z.; Wang, Y.H. Insight into the adsorption and dissociation of CH4 on Pt(h k l) surfaces: A theoretical study. *Appl. Surf. Sci.* **2012**, *258*, 7154–7160. [CrossRef]
26. Qi, D.; Luo, X.; Yao, J.; Yao, Y.; Lu, X. Computational study of CO catalytic oxidation on $Pd_{38}$ cluster model and Pd slab model. *J. Fuel Chem. Technol.* **2020**, *48*, 9.
27. Wang, D.S.; Li, Y.D. Bimetallic Nanocrystals: Liquid-Phase Synthesis and Catalytic Applications. *Adv. Mater.* **2011**, *23*, 1044–1060. [CrossRef] [PubMed]